Earthquake magnitude calculation without saturation from the scaling of peak ground displacement

Diego Melgar[1], Brendan W. Crowell[2], Jianghui Geng[3], Richard M. Allen[1], Yehuda Bock[3], Sebastian Riquelme[4], Emma M. Hill[5], Marino Protti[6], and Athanassios Ganas[7]

[1]Seismological Laboratory, University of California, Berkeley, California, USA, [2]Department of Earth and Space Sciences, University of Washington, Seattle, Washington, USA, [3]Cecil H. and Ida M. Green Institute of Geophysics and Planetary Physics, Scripps Institution of Oceanography, University of California, San Diego, La Jolla, California, USA, [4]Centro Sismológico Nacional, Universidad de Chile, Santiago, Chile, [5]Earth Observatory of Singapore, Nanyang Technological University, Singapore, [6]Observatorio Vulcanológico y Sismológico de Costa Rica, Universidad Nacional, Heredia, Costa Rica, [7]National Observatory of Athens, Athens, Greece

Abstract GPS instruments are noninertial and directly measure displacements with respect to a global reference frame, while inertial sensors are affected by systematic offsets—primarily tilting—that adversely impact integration to displacement. We study the magnitude scaling properties of peak ground displacement (PGD) from high-rate GPS networks at near-source to regional distances (~10–1000 km), from earthquakes between M_w6 and 9. We conclude that real-time GPS seismic waveforms can be used to rapidly determine magnitude, typically within the first minute of rupture initiation and in many cases before the rupture is complete. While slower than earthquake early warning methods that rely on the first few seconds of *P* wave arrival, our approach does not suffer from the saturation effects experienced with seismic sensors at large magnitudes. Rapid magnitude estimation is useful for generating rapid earthquake source models, tsunami prediction, and ground motion studies that require accurate information on long-period displacements.

1. Introduction

To develop reliable earthquake early warning (EEW) methods, and for many projects that aim toward earthquake preparedness, it is critical that we quantify the relationship between ground motion and earthquake source parameters (source-scaling laws). In the time domain, typical metrics of ground motion include peak ground acceleration, effective peak ground acceleration, peak ground velocity, and peak ground displacement (PGA, EPGA, PGV, and PGD, respectively). Frequency domain metrics include predominant periods [*Böse et al.*, 2014] as well as spectral accelerations, velocities, and displacements [*Douglas*, 2003]. Databases of recorded ground motions for earthquakes of different magnitudes and distance ranges are synthesized to these simpler parameters and then used for a broad suite of seismological applications.

A notable application of source-scaling laws is their use in EEW using relationships derived from the initial portion of the seismogram, typically a few (3–5) seconds after *P* wave arrivals. *Nakamura* [1988] studied the maximum predominant period of the *P* wave, *Wu and Kanamori* [2005] the predominant period, and *Wu and Zhao* [2006] the peak displacement. These studies computed scaling laws for these parameters as a function of earthquake magnitude that are used for operational warning around the world [*Allen et al.*, 2009]. Importantly, near-source tsunami warning systems rely on seismically derived hypocenters and magnitude computations to guide warning [*Hoshiba and Ozaki*, 2014], since deep-water measurements of the tsunami are typically not available for many tens of minutes after the onset of the event.

Another example of the application of source-scaling laws is in engineering seismology; ground motion parameters are of primary interest for fundamental problems such as the elaboration of ground motion prediction equations (GMPEs) [*Abrahamson et al.*, 2014]. GMPEs predict ground motion intensity parameters at a given location as a function of magnitude, distance to the source, and local site conditions, or for design spectra computation [*Chopra*, 2007]; these are important for developing building codes and seismic hazard assessments [*Panza et al.*, 2011].

Common to these applications is a strict reliance on inertial seismometers. The limitations of strong motion sensors in particular are well known; permanent coseismic displacements are hard to determine unambiguously [*Boore and Bommer*, 2005], and "baseline offsets"—caused primarily by unmodeled tilting—can affect the entire long-period band of the seismogram up to periods as high as 10 s [*Melgar et al.*, 2013] making measurements of not just coseismic offsets but also long-period surface and body waves unreliable. Band-pass filters are used to circumvent these issues; for example, the Next Generation Attenuation Relationships for Western US NGA-West2 project, which is charged with producing advanced GMPEs for the West Coast of the U.S., band-pass filters the accelerograms to maintain consistency across all records [*Ancheta et al.*, 2014]. In real-time applications such as EEW, high-pass filters with a corner period of 13 s are the norm [*Wu and Zhao*, 2006; *Hoshiba and Iwakiri*, 2011]. For large earthquakes, some higher-order source modeling products such as real-time distributed moment tensor sources also rely on high-pass filtered strong motion data [*Guilhem et al.*, 2013].

Many source-scaling laws and source models suffer from magnitude saturation effects due to removal of the long-period band of seismic records. *Kamai and Abrahamson* [2014] produced composite deterministic and stochastic synthetic waveforms for numerous finite fault rupture scenarios and then filtered them in the standard way described by *Ancheta et al.* [2014]. They noted that PGA scaling was unaffected by this processing since it is typically observed at higher frequencies and is not necessarily indicative of the source process. However, PGV, EPGA, and especially PGD are systematically underestimated after the records are filtered. This is unsurprising; the filtering operation removes the one-sided long-period velocity pulse that amplifies PGV and the coseismic offset and long-period surface waves which contribute substantially to the PGD measurement [*Crowell et al.*, 2013].

From the Kalman filter combination of collocated GPS and strong motion sensors, dubbed "seismogeodetic" combination [*Bock et al.*, 2011; *Geng et al.*, 2013], *Crowell et al.* [2013] found that magnitude saturation in scaling laws improved substantially, since the band-pass operation was no longer required. Notably, from the seismogeodetic combination for three large events *Crowell et al.* [2013] first noted the potential for PGD scaling, as well as Pd scaling.

In the following we will present results from an analysis of the scaling properties of PGD as measured by high-rate (sampled at 1 Hz or higher) GPS recordings at regional distances from ten moderate to large earthquakes. Since GPS is noninertial and measured with respect to an absolute reference frame, it is not affected by baseline offsets; it directly measures ground displacement, albeit with higher noise levels than strong motion sensors (typically 1–2 cm in the horizontal and 5 cm in the vertical). We conclude that the value of PGD scales as a function of magnitude at between M_w6 and 9 (at least) and at distances between 10 and 1000 km (where data have been recorded thus far). These observations have not been previously made with seismic data due to long-period information being absent from processed accelerograms and PGD being dependent on the filtering operation [*Boore and Bommer*, 2005]. We will further demonstrate how, if available, real-time GPS recordings can be used to rapidly determine the size of the source, typically within the first minute of rupture initiation and in many cases before the rupture is complete. While slower than EEW methods that rely on the first few seconds of the *P* wave, this method is more reliable since it does not suffer from saturation at large magnitudes and can be directly used for prompt assessment of the earthquake source and tsunami hazard.

2. Data and Methods

We collected data for 10 large events (Table 1 and Figure 1) that cover a magnitude range from M_w5.9 to M_w9.1 and were observed with high-rate GPS over the past decade. These events span a variety of tectonic regimes and faulting styles. The raw observations were processed to obtain displacement time series in local north, east, and up coordinates using the precise point positioning with ambiguity resolution algorithm of *Geng et al.* [2013], with a total of 1321 stations contributing to our analysis. The networks in Japan and the United States have significantly higher station density and contribute the largest portion of the records (Table 1). For every station-event pair, we computed the hypocentral distance (*R*) using the hypocenter location determined by the National Earthquake Information Centre (NEIC, http://earthquake.usgs.gov/). We removed the mean of 60 s of data before each event origin time (OT) to zero out the preevent portion of the record. PGD is then the peak dynamic displacement on the

Table 1. Details of the 10 Events Used in This Study

Event Name, Country	Epicentral Time[a] (UTC)	Moment (N m)	M_{PGD} With Vertical	M_{PGD} No Vertical	No. of GPS Sites Used	Kinematic Model Source
Tohoku-oki, Japan	2011-03-11 05:46:24	5.51×10^{22} (M_w9.09)	9.29 ± 0.31	9.27 ± 0.29	832	*Melgar and Bock* [2015]
Maule, Chile	2010-02-27 06:34:14	2.39×10^{22} (M_w8.85)	9.04 ± 0.32	9.06 ± 0.24	18	NEIC[b]
Tokachi-oki, Japan	2003-09-25 19:50:06	3.05×10^{21} (M_w8.25)	8.31 ± 0.32	8.30 ± 0.29	259	NEIC[b]
Iquique, Chile	2014-04-01 23:46:47	2.49×10^{21} (M_w8.19)	8.02 ± 0.31	7.96 ± 0.15	22	NEIC[b]
Mentawai, Indonesia	2010-10-25 14:42:22	4.60×10^{20} (M_w7.68)	7.41 ± 0.24	7.49 ± 0.22	10	NEIC[b]
Nicoya, Costa Rica	2012-09-05 14:42:08	2.93×10^{20} (M_w7.57)	7.50 ± 0.24	7.57 ± 0.27	9	NEIC[b]
El Mayor-Cucapah, Mexico	2010-04-04 22:40:42	7.60×10^{19} (M_w7.18)	7.39 ± 0.25	7.35 ± 0.23	108	*Uchide et al.* [2013]
Aegean Sea, Greece	2014-05-24 09:25:02	2.58×10^{19} (M_w6.87)	6.51 ± 0.22	6.58 ± 0.23	6	GCMT[c]
Napa, U.S.	2014-08-24 10:20:44	1.85×10^{18} (M_w6.11)	6.11 ± 0.17	6.07 ± 0.15	44	*Melgar et al.* [2015]
Parkfield, U.S.	2004-09-28 17:15:24	9.82×10^{17} (M_w5.92)	5.92 ± 0.13	5.97 ± 0.14	13	GCMT[c]

[a]Dates are formatted as year-month-day.
[b]Finite fault results for these events can be found at http://earthquakes.usgs.gov.
[c]We use the global CMT (GCMT) rise time as a measure of source duration. This can be found at http://www.globalcmt.org.

unfiltered GPS seismogram. The data may contain a static offset component or not (Figure 2); the definition is the same. We extract the PGD value from the three-component seismogram as

$$PGD = \max\left(\sqrt{\left[N(t)^2 + E(t)^2 + U(t)^2 \right]} \right); \qquad (1)$$

where $N(t)$, $E(t)$, and $U(t)$ are the north, east, and up displacement seismograms. We record the PGD value and the time after OT when it occurs. Figure 2 shows GPS waveforms that are representative of what we observe in the data set. Some waveforms are dominated by the coseismic ramp (Figures 2a and 2b), while others have large shaking superimposed on the coseismic offset (Figure 2c), and yet others have no appreciable coseismic offset and show only shaking (Figure 2d).
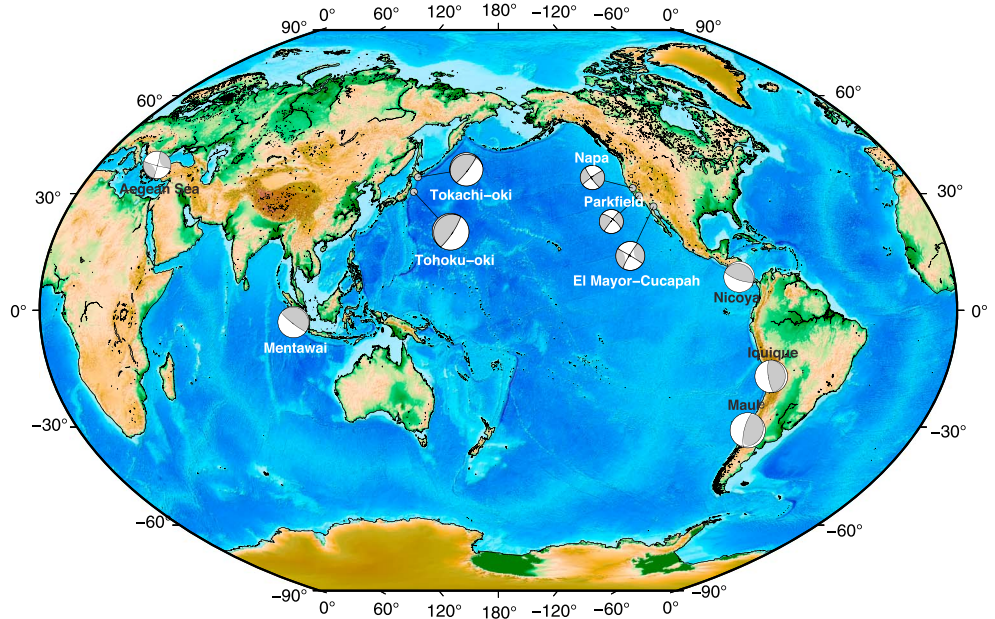

Figure 1. Centroid locations of the 10 events used in this study. Moment tensor solutions are from the Global Centroid Moment Tensor project (http://www.globalcmt.org/).
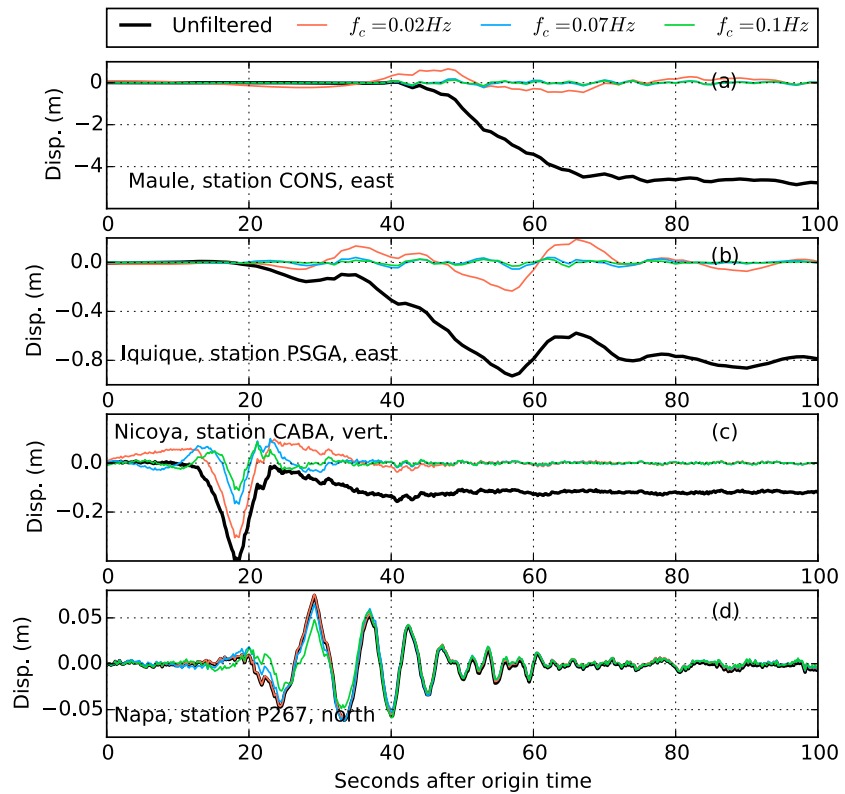
Figure 2. Sample GPS waveforms used in this study. The black lines are unfiltered displacement time series used for PGD calculation. The colored lines show the waveforms filtered with different five-pole Butterworth high-pass filters. The filter corners (f_c) are those typically used when processing accelerograms [e.g., *Kamai and Abrahamson*, 2014]. The results illustrate how PGD computations with filtered displacement data will ultimately underestimate its value and lead to saturation.

We use the scaling law proposed by *Crowell et al.* [2013] for PGD which includes magnitude-dependent attenuation to account for the relative strengths of the near-, intermediate-, and far-field seismic radiation terms

$$\log(\text{PGD}) = A + B \cdot M_w + C \cdot M_w \cdot \log(R). \qquad (2)$$

where A, B, and C are the regression coefficients, M_w is moment magnitude, and R is the source to station distance.

From the 1321 PGD measurements, and using the earthquake magnitudes for each event determined from finite fault inversions or centroid moment tensor (CMT) calculations (Table 1), we perform the regression for coefficients A, B, and C using an L1-norm minimizing solver that does not have strong sensitivity to outliers [*Shearer*, 1997]. The data from each earthquake are weighted by the norm of the vector of all its PGD values. This is necessary to keep events with more PGD measurements from dominating the inversion; in this way each earthquake is weighted equally in the regression. The uncertainties of the regression parameters cannot be directly calculated for an L1-norm minimizing inversion. We therefore estimate them using a bootstrap approach where we randomly remove 10% of the PGD measurements and rerun the regression. We repeated this procedure 1000 times to estimate the variance of the coefficients. Once the variance is known, we can present the uncertainties as the 95% confidence intervals of each coefficient.

Once the regression coefficients have been determined, we retrospectively analyze the time series to determine how quickly magnitude could have been determined had the scaling law been known at the time of the event. At 1 s intervals, and assuming that there is an estimate of the event location (which will be true if an EEW system is present in the area), we apply the regression to the observed PGDs at all sites and solve for magnitude. We test three traveltime masks at 2, 3, and 4 km/s for this magnitude calculation. An imaginary spherical
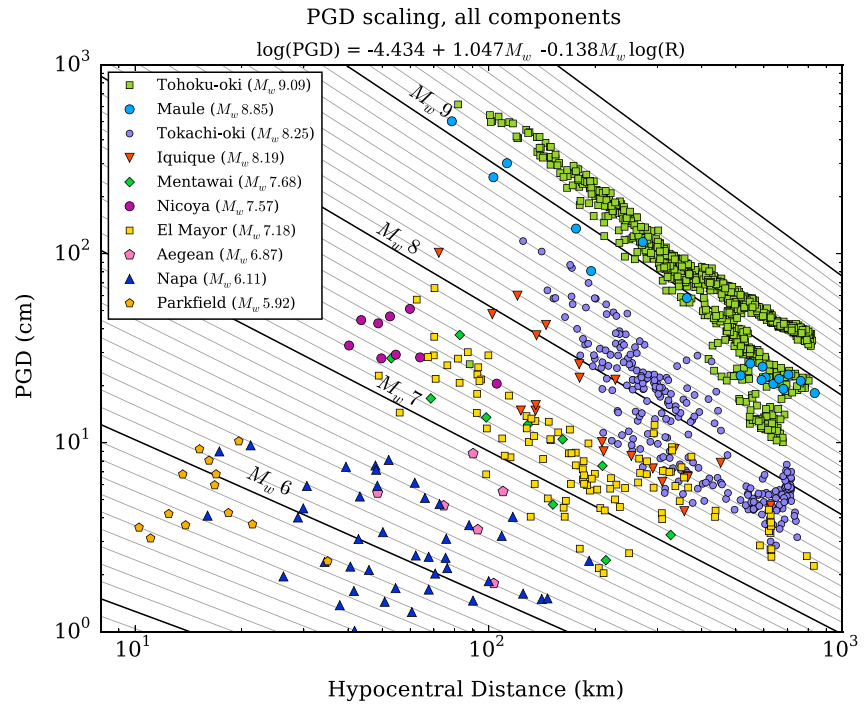
Figure 3. Scaling of peak ground displacement measurements (PGD). The oblique lines are the predicted scaling values from the L1 regression of the PGD measurements as a function of hypocentral distance.

wavefront radiates outward from the source, and only stations within this travel-time mask are included in the magnitude calculation. In this way, stations far away that are recording noise before seismic motions occur are kept from contaminating the calculation. This is also in keeping with the idea that PGD will occur once the static offset, which travels at S wave speed [e.g., *Grapenthin et al.*, 2014], is fully developed.

3. Results

The PGD measurements for all events are shown in Figure 3. The regression coefficients computed are $A = -4.434 \pm 0.141$, $B = 1.047 \pm 0.022$, and $C = -0.138 \pm 0.003$, and the standard error of the magnitude residuals is 0.27 magnitude units. For most subduction zone events there are no records at hypocentral distances shorter than 80 km. The exception is the Nicoya, Costa Rica, event which has GPS stations on a peninsula directly over the source area [*Protti et al.*, 2014] and thus hypocentral distances as short as 40 km. These mostly reflect the depth of the source (30 km). The two large strike-slip events (North Aegean Sea, Greece, and El Mayor-Cucapah, Mexico) have PGD measurements between 50 and 900 km. Notably, the smaller strike-slip events (Parkfield and Napa in California), which occurred inside the GPS networks of the west coast of the U.S., were measured at quite short distances: 10 km for Parkfield and 18 km for Napa. The range of measured PGDs is from 1 cm to almost 6 m for the Maule, Chile, and Tohoku-oki, Japan, events.

The results of the retrospective magnitude calculations are shown in Figure 4. We plot the evolution of magnitude for three different traveltime masks. Uncertainties at each epoch are determined using the regression coefficient uncertainties. Superimposed on the plots are the source time functions for kinematic slip inversions of each event (Table 1) except for the Parkfield and Aegean Sea events, where we have used the rise time from their centroid moment tensor solutions as a proxy for duration. For the Tohoku-oki event, a preliminary magnitude of $M_w 8.5$ is computed within 60 s and a final magnitude of $M_w 9.1$ is reached by 100 s. Similarly, for the Maule earthquake an estimate of $M_w 8.8$ is reached by 50 s and a final magnitude of 9.0 by 90 s. For the remaining events with magnitudes larger than 6.8, final magnitudes are obtained within 60 s and in most cases before rupture is finished. For the smaller Parkfield and Napa earthquakes, magnitudes close to the final magnitude are obtained within 10 s and final stable solutions by 30 s. The Mentawai, Indonesia, and Aegean Sea, Greece, events are somewhat underestimated, while the
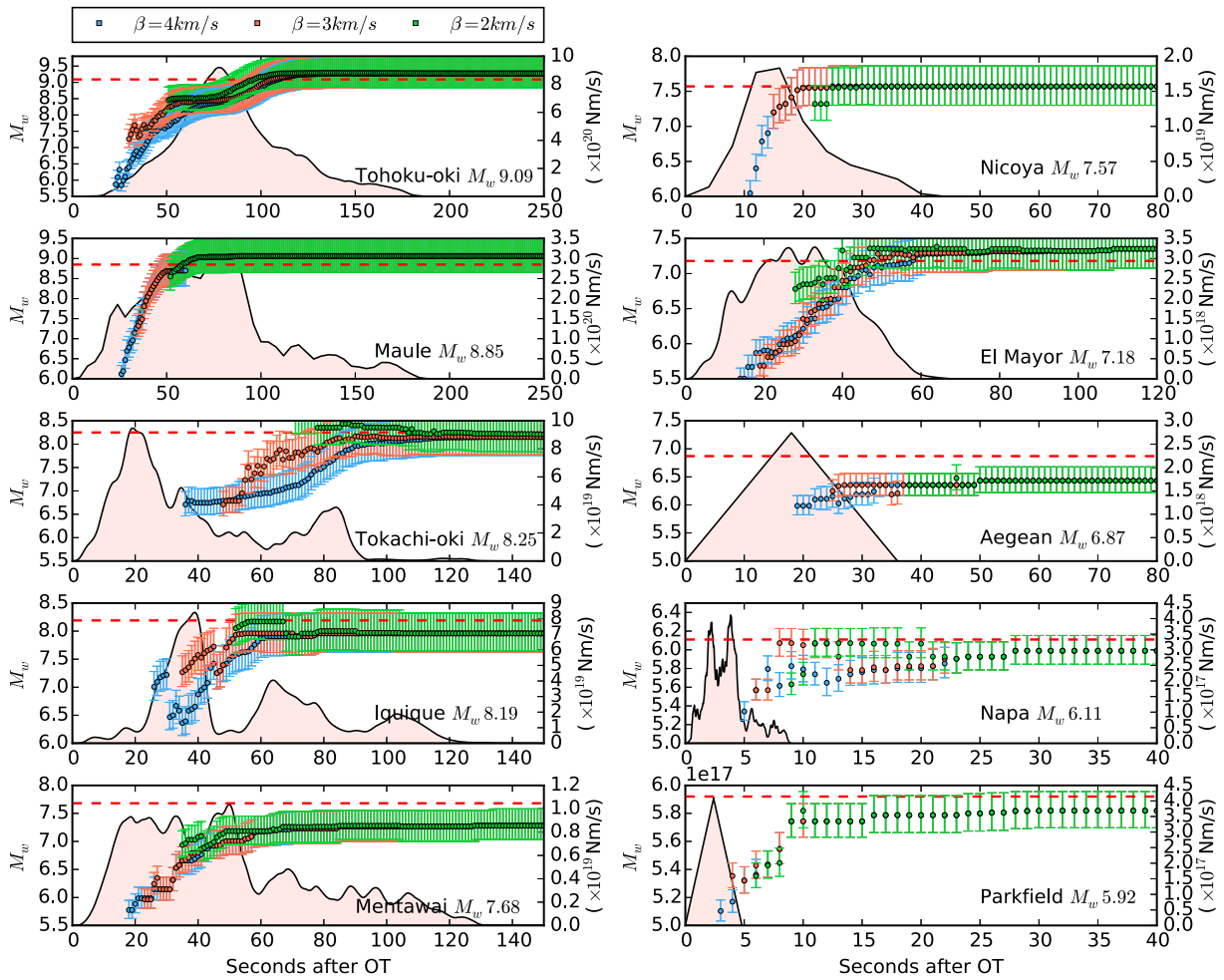
Figure 4. Retrospective analysis of the time evolution of magnitude using the scaling law of equation (1). Plotted are the magnitude calculations using three traveltime masks at 2, 3, and 4 km/s. The error bars are determined using the uncertainties of the regression coefficients. The red dashed line is the magnitude from the slip inversion (Table 1) for that event. The shaded pink regions are the source time functions for the kinematic slip inversions.

remaining events are close to the magnitudes determined by the post hoc finite fault or CMT solutions. To test whether the solutions are reliable only because we have included data for the event itself in the regression, we run the regressions and retrospective magnitude calculations again by sequentially removing each event from the calculation (Table S1 in the supporting information). We do not observe any significant bias.

4. Discussion

Figure 3 shows a clear scaling of PGD as a function of magnitude and hypocentral distance. For a particular source-station distance larger events will, in general, have larger values of PGD. This is perhaps unsurprising, as evidenced by the waveforms in Figure 2 and remarked upon in previous studies [*Crowell et al.*, 2013; *Melgar et al.*, 2013], since at regional distances from large events the displacement field can be largely dominated by the coseismic offset. This permanent displacement is the zero frequency (or DC) component of the radiated spectrum and as such is expected to scale directly with seismic moment. However, at intermediate distances the interplay between the coseismic offset and elastic waves will determine the value of PGD (Figure 2c, for example). As the coseismic offsets become negligible, long-period surface waves are expected to be the largest contributors to PGD. The distances at which this will happen will depend on the magnitude and radiation pattern of each event. The high-pass filtering of accelerograms not only eliminates the static offset but also dampens the peak amplitude of long-period surface waves (Figure 2) [*Melgar et al.*, 2013].

Figure 2 also illustrates how for moderate events such as the M_w6.1 Napa earthquake filtered strong motion records will likely accurately capture PGD. Roughly speaking, at regional distances M_w6 seems to be the lower threshold at which GPS begins to provide more accurate long-period ground motion estimates than inertial sensors [*Melgar et al.*, 2015].

For a given event the pattern of PGD can be complex, particularly at large distances. For the Tohoku-oki earthquake, the linear pattern of PGD values splits into three distinct trends at around 400 km; similar features are apparent for the Tokachi-oki and El Mayor-Cucapah earthquakes. This might reflect the geometry of the network with clustering of sites along preferred azimuths that will be affected preferentially by the source radiation pattern and underscores the importance of observing events from as many azimuths as possible. Similarly, this complexity might reflect the local Earth structure. At larger distances, and as the coseismic offsets become negligible, ground motions will have a larger contribution from local site effects. However, on average, the PGD values for each event scale well.

The low-magnitude calculations for the Aegean Sea (M_w6.58 versus M_w6.80) and Mentawai (M_w7.49 versus M_w7.68) events (Figure 4) are also evident in the PGD values for these earthquakes (Figure 3). In general, their values are low compared to those predicted by the scaling law. For the Mentawai earthquake this is particularly important. This event happened in the shallow portion of the megathrust, with slow rupture of compliant material as far as the shallow wedge [*Hill et al.*, 2012]. It is possible that the low PGD values reflect weak ground motion generation because of this; indeed, the event was not widely perceived by the local population [*Hill et al.*, 2012]. However, the Aegean Sea event involved supershear rupture of stronger material [*Evangelidis*, 2014] and yet also shows low values of PGD. An alternate explanation is that a single scaling law that explains global observations from different tectonic regimes is only a first-order approximation. As regional GPS networks record more events it will be possible to evaluate region-specific scaling laws and to determine whether the low PGD values for both of these events reflect characteristics of the source or if they simply require a region-specific model. Yet another explanation is possible; the vertical component of GPS recordings is typically 3–5 orders of magnitude noisier than the horizontal components. If we eliminate it from the regression and magnitude calculations (Figures S1 and S2), the uncertainties of the regression coefficients increase to $A = -4.639 \pm 0.170$, $B = 1.063 \pm 0.039$, and $C = -0.137 \pm 0.007$ and the standard error of the magnitude residual increases to 0.29 magnitude units. However, the magnitude computations for the Mentawai and Aegean Sea events improve substantially without degrading the computation for any of the other events. This may indicate that the low-magnitude estimates for these two events when using three-component data are due to high noise in the vertical time series and not a characteristic of the source process. Thus, it remains an operational decision whether to incorporate vertical time series into the computation and will largely depend on the known reliability and noise levels of a particular network. Potential improvements can include the collocation and real-time combination of seismic and geodetic sensors which significantly reduce noise levels in all channels and produce waveforms at the sensitivity of the accelerometer with frequency reliability down to 0 Hz [*Bock et al.*, 2011].

We also note that the magnitude computations shown here seem robust regardless of the number of sites used. For some of the events (Table 1) we have many tens to hundreds of stations contributing to retrospective magnitude determination. However, for others, for example, the Nicoya and Maule events, only a few stations contribute data, and in spite of this, magnitude determinations can still be made quickly.

Additionally, the impact of the travel-time masks is that of a trade-off between speed of the solution and accuracy. The faster traveltime mask (4 km/s) means data are used sooner and a solution is available more quickly, but the first magnitude values are underestimated. A slower travel-time mask will delay the computation but will result in the first magnitude estimates being closer to the final solution. Furthermore, we have assumed that although a rapid hypocentral determination is available, additional testing will determine the methods sensitivity to errors in hypocentral location.

Although this approach is fast, it is not as fast as P wave-based EEW algorithms. However, compared to seismic-only methods, it will not saturate and thus can be used to update EEW alerts. Furthermore, this simple algorithm for magnitude determination can be used as a first-order approach to tsunami warning. Currently, operational near-source warning systems rely on precomputed scenarios [*Hoshiba and Ozaki*, 2014] and they require a magnitude and location to seed a database query for the most likely scenario. This approach has the advantage of being very fast since no complex computation of tsunami propagation needs to be made,

although it is only as robust as the scenario earthquakes contained in its database. It has been well documented that during the 2011 M_w9.0 Tohoku-oki earthquake magnitude saturation led to an underestimate of the expected tsunami intensity [*Hoshiba and Ozaki*, 2014] and thus a warning level that was too low in the first hours. With PGD measurements from regional GPS sites, magnitude saturation becomes a nonissue, ensuring that the most realistic scenario is selected. Afterward, as the hazard unfolds and other geophysical measurements become available, more complex predictions of tsunami intensity from higher-order source products can be made [*Melgar and Bock*, 2013, 2015] and the warning can be refined.

Finally, the results discussed here also show that GPS time series could be of more widespread use in ground motion studies. There are now many thousands of recordings of large events from high-rate GPS time series. Typically, earthquake engineering studies rely only on accelerograms because seismic loadings (force-based design) are determined from PGA and PGV, which occur at higher frequencies [e.g., *Kamai and Abrahamson*, 2014]. However, there are many instances in which PGD and other displacement metrics need to be precisely known. For long-baseline structures such as bridges and skyscrapers, displacement-based design may be a better approach [i.e., *Kappos et al.*, 2013]. Displacement quantities such as PGD and response spectra with reliable information on long-period shaking are key design metrics but are not always well represented in accelerogram-derived calculations [*Melgar et al.*, 2013]. Base-isolated buildings, which are decoupled from the ground, experience less damage as shear forces are reduced and are widespread in some earthquake-prone areas. However, they experience large displacements relative to the ground; this increases the potential for impact (pounding) with nearby structures, potentially producing significant damage [*Pant and Wijeyewickrema*, 2012]. If long-period motions up to the coseismic offset are not well characterized, then there is potential for failures of design.

This study as well as previous work argues that the contribution of GPS to ground motion studies is not simply in the determination of the coseismic field but rather in the proper assessment of the entire long-period band of motion. Seismic data alone will have biases, and accelerograms with baseline offsets will be in error potentially at periods as high as 10 s [*Melgar et al.*, 2013]. These advantages can be further enhanced with seismogeodesy collocated GPS and strong motion sensors; GPS should be conceptualized as a noninertial long-period strong motion sensor and its measurements used accordingly. The GPS community maintains several databases of global high-rate GPS observations; however, these are raw data and not position time series. One of the challenges to be addressed by the geodetic community is to make processed position time series from large earthquakes more widely available to other Earth scientists and engineers. The processed waveforms used in this study are available in seismic formats from the Scripps Orbit and Permanent Array Center archive (http://sopac.ucsd.edu).

5. Conclusions

We have shown results from an analysis of the scaling properties of PGD as measured by high-rate GPS at regional distances from moderate to large earthquakes. GPS is noninertial and directly measures ground displacement. Furthermore, it is unaffected by baseline offsets that affect strong motion sensors. We find that PGD scales for at least the range M_w6 to 9 and at distances between 10 and 1000 km. We have demonstrated how, if available, real-time GPS recordings can be used to rapidly determine the size of the source without any concern for saturation, typically within the first minute of rupture initiation and in many cases before the rupture is complete. While slower than EEW methods that rely on the first few seconds of the P wave, this method is more reliable since it does not suffer from saturation at large magnitudes and can be directly used for prompt assessment of tsunami hazard. This study also underscores the utility of real-time GPS time series to rapidly characterize the source, assess the risk, and warn for tsunamis, and for ground motion studies that require accurate information on long-period displacements.

References

Abrahamson, N. A., W. J. Silva, and R. Kamai (2014), Summary of the ASK14 ground motion relation for active crustal regions, Earthquake Spectra NGA-West2 special issue.
Allen, R. M., P. Gasparini, O. Kamigaichi, and M. Böse (2009), The status of earthquake early warning around the world: An introductory overview, *Seismol. Res. Lett.*, *80*, 682–693, doi:10.1785/gssrl.80.5.682.
Ancheta, T. D., et al. (2014), NGA-West2 database, *Earthquake Spectra*, *30*(3), 989–1005.
Bock, Y., D. Melgar, and B. W. Crowell (2011), Real-time strong-motion broadband displacements from collocated GPS and accelerometers, *Bull. Seismol. Soc. Am.*, *101*(6), 2904–2925.

Boore, D. M., and J. J. Bommer (2005), Processing of strong-motion accelerograms: Needs, options and consequences, *Soil Dyn. Earthquake Eng.*, *25*(2), 93–115.

Böse, M., et al. (2014), CISN ShakeAlert: An earthquake early warning demonstration system for California, in *Early Warning for Geological Disasters*, pp. 49–69, Springer, Berlin.

Chopra, A. K. (2007), *Dynamics of Structures: Theory and Applications to Earthquake Engineering*, Pearson/Prentice Hall.

Crowell, B. W., D. Melgar, Y. Bock, J. S. Haase, and J. Geng (2013), Earthquake magnitude scaling using seismogeodetic data, *Geophys. Res. Lett.*, *40*, 6089–6094, doi:10.1002/2013GL058391.

Douglas, J. (2003), Earthquake ground motion estimation using strong-motion records: A review of equations for the estimation of peak ground acceleration and response spectral ordinates, *Earth Sci. Rev.*, *61*(1), 43–104.

Evangelidis, C. P. (2014), Imaging supershear rupture for the 2014 M_w6.9 Northern Aegean earthquake by backprojection of strong motion waveforms, *Geophys. Res. Lett.*, *42*, 307–315, doi:10.1002/2014GL062513.

Geng, J., Y. Bock, D. Melgar, B. W. Crowell, and J. S. Haase (2013), A new seismogeodetic approach to GPS and accelerometer observations of the 2012 Brawley seismic swarm: Implications for earthquake early warning, *Geochem. Geophys. Geosyst.*, *14*, 2124–2142, doi:10.1002/ggge.20144.

Grapenthin, R., I. A. Johanson, and R. M. Allen (2014), Operational real-time GPS-enhanced earthquake early warning, *J. Geophys. Res. Solid Earth*, *119*, 7944–7965, doi:10.1002/2014JB011400.

Guilhem, A., D. S. Dreger, H. Tsuruoka, and H. Kawakatsu (2013), Moment tensors for rapid characterization of megathrust earthquakes: The example of the 2011 *M* 9 Tohoku-oki, Japan earthquake, *Geophys. J. Int.*, *192*, 759–772.

Hill, E. M., et al. (2012), The 2010 M_w7.8 Mentawai earthquake: Very shallow source of a rare tsunami earthquake determined from tsunami field survey and near-field GPS data, *J. Geophys. Res.*, *117*, B06402, doi:10.1029/2012JB009159.

Hoshiba, M., and K. Iwakiri (2011), Initial 30 seconds of the 2011 off the Pacific coast of Tohoku earthquake (M_w9.0)—Amplitude and τ_c for magnitude estimation for earthquake early warning, *Earth Planets Space*, *63*, 553–557, doi:10.5047/eps.2011.06.015.

Hoshiba, M., and T. Ozaki (2014), Earthquake early warning and tsunami warning of the Japan Meteorological Agency, and their performance in the 2011 off the Pacific Coast of Tohoku earthquake (*M* 9.0), in *Early Warning for Geological Disasters*, pp. 1–28, Springer, Berlin.

Kamai, R., and N. Abrahamson (2014), *Are Near-Fault Fling Effects Captured in the New NGA West2 Ground Motion Models?*, Earthquake Spectra.

Kappos, A. J., K. I. Gkatzogias, and I. G. Gidaris (2013), Extension of direct displacement-based design methodology for bridges to account for higher mode effects, *Earthquake Eng. Struct. Dyn.*, *42*(4), 581–602.

Melgar, D., and Y. Bock (2013), Near-field tsunami models with rapid earthquake source inversions from land- and ocean-based observations: The potential for forecast and warning, *J. Geophys. Res. Solid Earth*, *118*, 5939–5955, doi:10.1002/2013JB010506.

Melgar, D., and Y. Bock (2015), Kinematic earthquake source inversion and tsunami runup prediction with regional geophysical data, *J. Geophys. Res. Solid Earth*, *120*, 3324–3349, doi:10.1002/2014JB011832.

Melgar, D., Y. Bock, D. Sanchez, and B. W. Crowell (2013), On robust and reliable automated baseline corrections for strong motion seismology, *J. Geophys. Res. Solid Earth*, *118*, 1177–1187, doi:10.1002/jgrb.50135.

Melgar, D., J. Geng, B. W. Crowell, J. S. Haase, Y. Bock, W. C. Hammond, and R. M. Allen (2015), Seismogeodesy of the 2014 M_w6.1 Napa earthquake, California: Rapid response and modeling of fast rupture on a dipping strike-slip fault, *J. Geophys. Res. Solid Earth*, doi:10.1002/2015JB011921.

Nakamura, Y. (1988), On the urgent earthquake detection and alarm system (UrEDAS), Presented at the Ninth World Conf. Earthq. Eng., Tokyo.

Pant, D. R., and A. C. Wijeyewickrema (2012), Structural performance of a base-isolated reinforced concrete building subjected to seismic pounding, *Earthquake Eng. Struct. Dyn.*, *41*(12), 1709–1716.

Panza, G. F., K. Irikura, M. Kouteva, A. Peresan, Z. Wang, and R. Saragoni (2011), Advanced seismic hazard assessment, *Pure Appl. Geophys.*, *168*(1–2), 1–9.

Protti, M., V. González, A. V. Newman, T. H. Dixon, S. Y. Schwartz, J. S. Marshall, and S. E. Owen (2014), Nicoya earthquake rupture anticipated by geodetic measurement of the locked plate interface, *Nat. Geosci.*, *7*(2), 117–121.

Shearer, P. M. (1997), Improving local earthquake locations using the L1 norm and waveform cross correlation: Application to the Whittier Narrows, California, aftershock sequence, *J. Geophys. Res.*, *102*(B4), 8269–8283, doi:10.1029/96JB03228.

Uchide, T., H. Yao, and P. M. Shearer (2013), Spatio-temporal distribution of fault slip and high-frequency radiation of the 2010 El Mayor-Cucapah, Mexico earthquake, *J. Geophys. Res. Solid Earth*, *118*, 1546–1555, doi:10.1002/jgrb.50144.

Wu, Y. M., and H. Kanamori (2005), Experiment on an onsite early warning method for the Taiwan early warning system, *Bull. Seismol. Soc. Am.*, *95*, 347–353, doi:10.1785/0120040097.

Wu, Y. M., and L. Zhao (2006), Magnitude estimation using the first three seconds *P*-wave amplitude in earthquake early warning, *Geophys. Res. Lett.*, *33*, L16312, doi:10.1029/2006GL026871.